Post-Buckled Precompressed Techniques in Adaptive Aerostructures: An Overview

Roelof Vos
Assistant Professor
Mem. ASME
Faculty of Aerospace Engineering,
Delft University of Technology,
2600 GB Delft, The Netherlands
e-mail: r.vos@tudelft.nl

Ron Barrett
Associate Professor
Mem. ASME
Department of Aerospace Engineering,
University of Kansas,
Lawrence, KS 66045
e-mail: barrettr@ku.edu

An overview of the development and application of post-buckled precompressed (PBP) piezoelectric actuators is presented. It has been demonstrated that PBP actuators outperform conventional piezoelectric actuators by relying on axial compression to counter the inherent stiffness in the actuator element. In doing so, the mechanical work output has been shown to increase threefold compared with conventional bimorph actuators. Actuator stroke has been demonstrated to increase up to 300% without compromising the blocked force capability. This has resulted in an expansion of the design space of piezoelectric bender elements and has made them excellent candidates for potentially replacing certain classes of conventional electromechanical flight control actuators. The successful application of PBP elements can be found in unmanned aerospace systems ranging from subscale vertical-take-off-and-landing vehicles to supersonic missile fins. With respect to conventional electromechanical servoactuators, it is demonstrated that PBP actuator elements induce a lower systems weight fraction, a substantially higher bandwidth, and an order of magnitude lower power consumptions and part count.
[DOI: 10.1115/1.4001202]

1 Introduction

Although there are quite a number of aircraft applications that rely on adaptive materials for sensor or actuator purposes (many in the uninhabited aerial vehicle (UAV) and remote control (R/C) aircraft category), there are fewer examples of applications where adaptive material actuators were used for primary flight control [1,2]. Most commonly used adaptive materials that qualify for these tasks are shape memory alloy (SMA) and piezoelectric actuators. Even though SMA possesses the highest single-stroke energy density of all current adaptive materials, its lack in bandwidth and high hysteresis are significant drawbacks when it comes to applying these materials in flight control actuators. Furthermore, its high power consumption typically leads to heavy secondary systems (e.g., power supply), which is undesirable, especially for subscale UAVs because of their relatively tight system weight constraints.

Piezoelectric actuators, on the other hand, have a very high bandwidth and a comparatively low power consumption. Traditionally, the major drawback in applying piezoelectric actuators lay in their limited stroke capacity at a given blocked force. To tackle this problem, several piezoelectric actuator arrangements have been devised to increase the mechanical stroke by using linkages or nonconventional actuator arrangements. In 1996, flexural amplification hinges were introduced that amplified the small displacement of a piezoelectric stack actuator. A variety of topologies were investigated ranging from simple lever mechanisms to four-bar linkage amplifiers [3]. It was shown that these mechanisms could increase stroke significantly with appropriate accuracy, but at the expense of force output. A similar concept relying on mechanical amplification by means of a lever arm was applied in a helicopter blade to deploy a vortex generator that tripped the boundary layer to delay separation [4]. In 1997, cymbal actuators were developed that magnified the expansion and contraction of a circular piezoelectric actuator by sandwiching it between two truncated conical end caps. The actuation of the piezoelectric disk resulted in an amplified through-the-thickness motion of the end caps that was 40 times larger than that of the lead titanate zirconate (PZT) itself. In 1999, the so-called x-frame amplification scheme was introduced, where piezoelectric stacks reacted against an inert frame of relatively low mass to amplify the small displacements of the stacks [5]. This actuator scheme was designed to control a rotorblade servoflap to improve vibration, acoustics, and aerodynamic performance. To increase the amplification even further, a double-lever amplification mechanism for piezoelectric stacks was shown to magnify the displacements by a factor of 21 [6]. Two L-shaped levers were connected in series to a piezostack, while the whole mechanism was embedded in a rigid frame.

In 1996, a tapered piezoelectric bender element was constructed to actuate a servoflap on a helicopter rotor blade [7]. Connected by flexural hinges, the tip deflection of the cantilevered bender element was shown to reach 11.5 deg under no-load conditions at frequencies of up to 100 Hz. It was demonstrated that tapering the piezoelectric bender element could increase the efficiency with which the available strain energy was converted into mechanical work at the tip. Other incarnations relied on the initial displacement of a buckled beam, which was amplified by a variable axial force of the piezoelectric stack actuator [8,9]. Another example of an arrangement that bridges the gap between the small displacement of stack actuators and the low blocked force capability of bender elements is the C-block actuator [10,11]. This C-block actuator is a semicircular composite bender actuated with piezoelectric layers. It was demonstrated that the work output of a C-block actuator could be increased with 8% with respect to a similar straight bender actuator [12]. Furthermore, blocked force capability increased with a factor of 2.7, and displacement reduced with a factor of 0.4, positioning the C-block actuator somewhere in between the bender and stack actuators.

Even though these measures have been proven to properly increase the effective stroke, many amplification mechanisms simultaneously reduced the blocked force capability. Due to finite friction in hinges or the dissipation of energy in flexural hinges, this often resulted in lower effective energy densities and reductions in total work output. Moreover, many of the amplification schemes required the addition of stiff (heavy) frames and lever arms to achieve the required level of amplification. In an effort to simultaneously increase the mechanical stroke and the blocked force

Contributed by the Mechanisms and Robotics Committee of ASME for publication in the JOURNAL OF MECHANICAL DESIGN. Manuscript received October 6, 2008; final manuscript received February 1, 2010; published online March 19, 2010. Assoc. Editor: Mary Frecker.

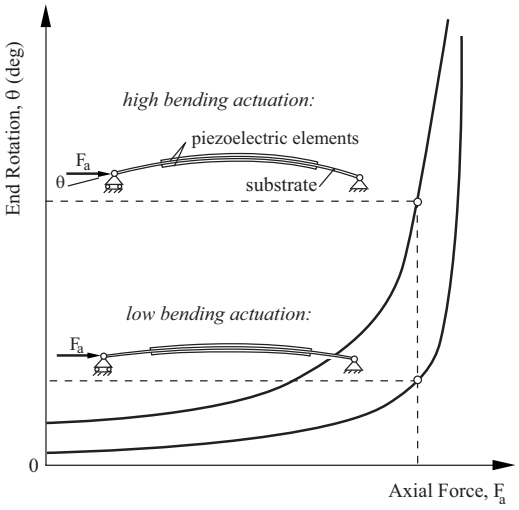

Fig. 1 Operating principle of PBP actuator [14]

capability, a novel mechanism was invented that essentially nullified the passive stiffness of the actuator element [13]. This resulted in higher a mechanical work output, which consequently increased the energy density of the baseline piezoelectric actuator.

To reduce the passive stiffness of the actuator element, an external end force close to its perfect-column buckling load was applied to the actuator element. By doing so, each bending imperfection that was introduced by the piezoelectric actuator element was effectively magnified by the axial force. The actuator element that relied on this principle was termed post-buckled precompressed (PBP), and its development and aerospace applications are the subject of this article. The mechanism of magnification of initial bending imperfections is schematically displayed in Fig. 1, along with the corresponding axial force versus end rotation graph. Note that the end rotation of the PBP actuator is a measure for the actuator stroke that was referred to earlier. If the graph of Fig. 1 is observed, one can see the profound effect that the addition of an axial load has on the end rotation of the actuator element. Because of the increased mechanical stroke along with an increase in blocked force capability, the design space of conventional bimorph actuators can be significantly enlarged when axial compression is used to decrease the passive stiffness of the actuator element.

2 Analytic Modeling of PBP Actuator Elements

2.1 Bimorph Piezoelectric Actuator Elements. The active component in the PBP actuator element that is considered in this section comprises of a bimorph piezoelectric actuator element. This actuator consists of two piezoelectric sheets that are bonded to either side of a thin substrate by means of an adhesive. The piezoelectric elements are electrically connected, such that when an electric field is applied, the top and bottom elements strain in the opposite direction. This introduces a curvature in the beam, which can, in turn, be used to perform mechanical work. A schematic representation of such a bimorph actuator element is presented in Fig. 2.

To relate the electric field strength E_3 to the curvature κ, the classical laminated plate theory (CLPT) is used. The strain Λ that is introduced in the piezoelectric elements is related through the piezoelectric charge constant d_{3i}, $i=1,2,3$, assuming a linear model: $\Lambda_i=d_{3i}E_3$. This introduces moments within the actuator laminate, which can be calculated by using the classical laminated plate theory [15]

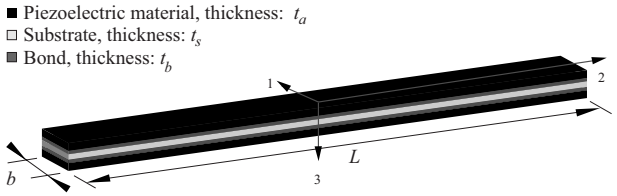

Fig. 2 Bimorph piezoelectric actuator element

$$\begin{pmatrix} M_1 \\ M_2 \\ M_{12} \end{pmatrix} = \left[\begin{array}{ccc|ccc} B_{11} & B_{12} & B_{16} & D_{11} & D_{12} & D_{16} \\ B_{12} & B_{22} & B_{26} & D_{12} & D_{22} & D_{26} \\ B_{16} & B_{26} & B_{66} & D_{16} & D_{26} & D_{66} \end{array}\right]_a \begin{pmatrix} \Lambda_1 \\ \Lambda_2 \\ 0 \\ 0 \\ 0 \\ 0 \end{pmatrix}_a \tag{1}$$

For most monolithic piezoceramic materials, $d_{31}=d_{32}$, and therefore $\Lambda=\Lambda_1=\Lambda_2=d_{31}E_3$, again, assuming a linear or only second-order induced-strain model.

The moments induced by the actuator elements are balanced by the strains ε and curvatures κ in the laminate. In this analysis, the curvature is of interest, which relates to the moment according to

$$\begin{pmatrix} M_1 \\ M_2 \\ M_{12} \end{pmatrix} = \left[\begin{array}{ccc|ccc} B_{11} & B_{12} & B_{16} & D_{11} & D_{12} & D_{16} \\ B_{12} & B_{22} & B_{26} & D_{12} & D_{22} & D_{26} \\ B_{16} & B_{26} & B_{66} & D_{16} & D_{26} & D_{66} \end{array}\right]_l \begin{pmatrix} \varepsilon_1 \\ \varepsilon_2 \\ \varepsilon_{12} \\ \kappa_1 \\ \kappa_2 \\ \kappa_{12} \end{pmatrix}_l \tag{2}$$

The bimorph laminate consists of isotropic and quasi-isotropic laminae. The laminate is balanced and symmetric, and the coefficients in the $[B]_l$ matrix are therefore all zero. The curvatures induced in the element can now be obtained by equating the moments produced by the actuator elements to the bending moments in the beam

$$\begin{pmatrix} \kappa_1 \\ \kappa_2 \\ \kappa_{12} \end{pmatrix}_l = \begin{bmatrix} D_{11} & D_{12} & D_{16} \\ D_{12} & D_{22} & D_{26} \\ D_{16} & D_{26} & D_{66} \end{bmatrix}_l^{-1} \begin{bmatrix} B_{11} & B_{12} & B_{16} \\ B_{12} & B_{22} & B_{26} \\ B_{16} & B_{26} & B_{66} \end{bmatrix}_a \begin{pmatrix} \Lambda \\ \Lambda \\ 0 \end{pmatrix}_a \tag{3}$$

The curvature about the 1-axis is of most interest for actuation purposes and can be closely approximated by simplifying Eq. (3) according to

$$\kappa = \kappa_1 = \frac{(B_{11}+B_{12})_a}{(D_{11}+D_{12})_l}\Lambda = \frac{B_a}{D_l}\Lambda \tag{4}$$

where D_l is the distributed bending stiffness of the laminate and B_a is the distributed coupling stiffness of the actuator elements. Using CLPT and the laminate definitions of Fig. 2, these coefficients can be explicitly expanded.

2.2 Model of Quasi-Static Behavior of PBP Actuators. In the buckled mode, the relation between the end rotation and axial force was investigated extensively [16–18]. In a simply supported configuration, the PBP element can be used to provide a moment and rotation to an aerodynamic surface, e.g., a grid fin on a subscale convertible UAV [16]. An additional moment results in the arrangement, as laid out in Fig. 3. By using the unloaded laminate curvature κ as a starting point, the problem can now be defined in terms of gross curvatures with an externally applied axial force and moment, F_a and M_{ex}, respectively.

Using the Euler–Bernoulli beam theory and inserting the CLPT nomenclature, the moment in the PBP element is found from

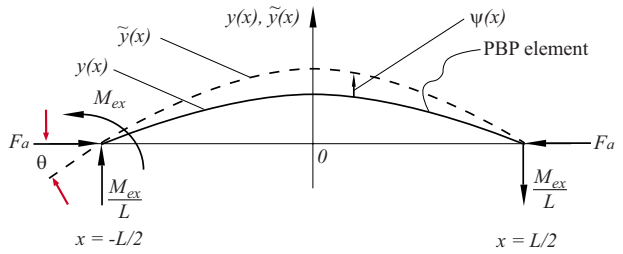

Fig. 3 Terms and conventions for analysis of the PBP actuator arrangement

$$M = D_l b \frac{d^2\psi}{dx^2} \tag{5}$$

where $\psi = \tilde{y} - y$ is the difference between the initial displacement function and the displacement induced by the axial force. From the geometry (see Fig. 3), the moment in the beam can be calculated according to

$$M = -F_a(\psi + y) + M_{\text{ex}}\left(\frac{x}{L} - \frac{1}{2}\right) \tag{6}$$

Combining Eqs. (5) and (6), the following equilibrium is found:

$$D_l b \frac{d^2\psi}{dx^2} = -F_a(\psi + y) + M_{\text{ex}}\left(\frac{x}{L} - \frac{1}{2}\right) \tag{7}$$

Rearranging results in the following second-order differential equation in ψ:

$$\psi'' + \frac{F_a}{D_l b}\psi = -\frac{F_a}{D_l b}y + \frac{M_{\text{ex}}}{D_l b}\left(\frac{x}{L} - \frac{1}{2}\right) \tag{8}$$

Solving this differential equation for ψ and adding the solution to $y(x)$ (as shown explicitly by Vos et al. [19]) results in the following mode shape for the actuator element:

$$\tilde{y} = \kappa \frac{D_l b}{F_a} \frac{\cos\left(\sqrt{\frac{F_a}{D_l b}}x\right)}{\cos\left(\sqrt{\frac{F_a}{D_l b}}\frac{L}{2}\right)} + \frac{M_{\text{ex}}}{2F_a}\left[\frac{\cos\left(\sqrt{\frac{F_a}{D_l b}}x\right)}{\cos\left(\sqrt{\frac{F_a}{D_l b}}\frac{L}{2}\right)} - \frac{\sin\left(\sqrt{\frac{F_a}{D_l b}}x\right)}{\sin\left(\sqrt{\frac{F_a}{D_l b}}\frac{L}{2}\right)}\right] + \frac{M_{\text{ex}}}{F_a}\left(\frac{x}{L} - \frac{1}{2}\right) \tag{9}$$

Taking the derivative of this shape function and evaluating the result at $x = -L/2$ results in the end rotation θ

$$\theta = \tan^{-1}\left\{\kappa\sqrt{\frac{D_l b}{F_a}}\tan\left(\sqrt{\frac{F_a}{D_l b}}\frac{L}{2}\right) - \frac{M_{\text{ex}}}{2F_a}\sqrt{\frac{F_a}{D_l b}}\left[\frac{1}{\tan\left(\sqrt{\frac{F_a}{D_l b}}\frac{L}{2}\right)} - \tan\left(\sqrt{\frac{F_a}{D_l b}}\frac{L}{2}\right)\right] + \frac{M_{\text{ex}}}{LF_a}\right\} \tag{10}$$

For a given external moment and axial force, Eq. (10) presents the end rotation to the pivot as a function of the initial induced curvature κ. By substituting $\kappa = \kappa(E_{3,\max})$ and $\kappa = \kappa(-E_{3,\max})$, and subsequently subtracting the latter result from the first result, yields the peak-to-peak end rotation

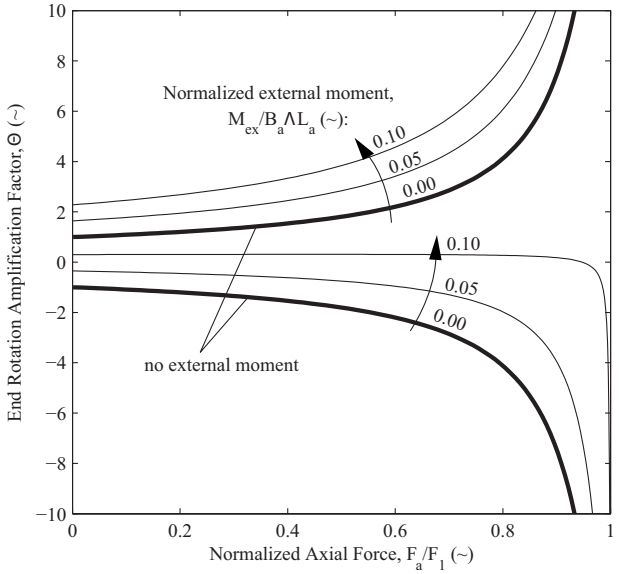

Fig. 4 End rotation amplifications due to axial compression as predicted by Eq. (10) for various applied moments

$$\theta_{p2p} = \tan^{-1}\left\{2\kappa\sqrt{\frac{D_l b}{F_a}}\tan\left(\sqrt{\frac{F_a}{D_l b}}\frac{L}{2}\right)\right\} \tag{11}$$

From Eq. (11), it is obvious that the external moment does not have any effect on the range of end rotations, it only offsets it.

2.2.1 Effect of Axial Force. In Fig. 4, the normalized end rotation $\Theta = \theta/\theta_{F_a=0}$ is plotted for the increasing values of axial force and various blocked moments. The axial force is normalized with respect to the perfect-column buckling load F_1. It can be seen that the amplification of the original end rotation at $F_a = 0$ increases exponentially with the applied axial load. In theory, when the axial force approaches F_1, the end rotations become unbounded. In reality, however, there is a tensile failure boundary that should be put in place. At this boundary, the curvature in the PBP element becomes so large that tensile failure (e.g., fracture or depoling) of the convex elements occurs. The present analysis does not include a boundary for tensile failure. However, this topic is discussed in Sec. 3.2.

2.2.2 Effect of External Moment. The two thicker lines in Fig. 4 show the maximum and minimum (normalized) end rotations for a given PBP actuator with no external moment applied. The end rotations are equal in magnitude and opposite in direction. The effect of the externally applied moment is that the lines shift upwards, resulting in higher end rotations in the direction of the applied moment. In this graph, the blocked moments are normalized with respect to the distributed moment multiplied by the length of the bender element ($B_a \Lambda L$), which is constant for a given geometry and electric field. The shifting of the lines is due to the effect that the external moment is helping the actuator to deflect in one direction, while it is opposing the element in the opposite direction. When the external moment continues to grow, at some point, the actuator element is not capable of generating the required opposite moment to push it through the neutral position to the opposite side. In that case, the end rotation θ does not switch its sign, but stays in the positive realm, even when axial loads are increased.

2.3 Model of Dynamic Behavior of PBP Actuators. In the dynamic analysis of PBP actuator elements, the influence of the axial load on the bandwidth of the actuator is investigated. The reader is asked to consider the simply supported PBP element of

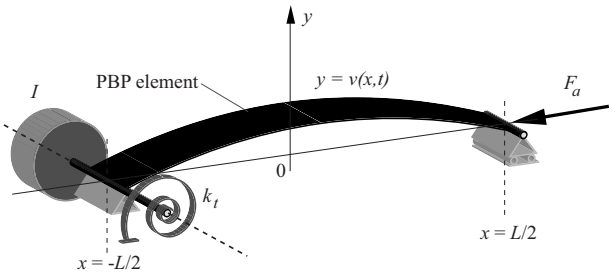

Fig. 5 Model problem for the dynamic analysis of PBP actuator elements

Fig. 5. An axial force F_a is present that magnifies the initial imperfections in the beam. In addition, a lumped inertia I and a linear torsional spring of stiffness k_t are added to one of the pivots.

In this analysis, structural damping is neglected. The displacement function $v(x,t)$ is substituted by a product of a shape function $\phi(x)$ and an amplification function depending on time $z(t)$

$$v(x,t) = \phi(x)z(t) \tag{12}$$

Actuation stems from a distributed moment that is introduced by a time dependent electric field in the through-the-thickness direction $B_a d_{31} E_3(t)$. The average density of the PBP actuator ρ is a weighted average of the constituent material densities

$$\rho = \frac{2\rho_a t_a + 2\rho_b t_b + \rho_s t_s}{2t_a + 2t_b + t_s} \tag{13}$$

Using a virtual work approach and using the Euler–Bernoulli beam assumptions, the following equation of motion for an axially loaded PBP element can be found:

$$M\ddot{z} + Kz = G(t) \tag{14}$$

with

$$M = \left[\rho \int_0^L \phi^2(x)dx\right] + I\tan^{-1}[\phi'(-L/2)]$$

$$K = \left[\int_0^L D_l(\phi''(x))^2 - \frac{F}{b}(\phi'(x))^2 dx\right] + k_t \tan^{-1}[\phi'(-L/2)]$$

$$G(t) = B_a d_{31} E_3(t)\left[\int_0^L \phi''(x)dx\right]$$

For the simply supported PBP element, a sinusoidal shape function is chosen

$$\phi(x) = \sin(\pi x/L) \tag{15}$$

When a harmonic forcing function with a forcing frequency of ω is chosen for the electric field strength, the following normalized response can be found:

$$X_{\text{norm}} = \left[1 - \omega^2 \frac{\rho \int_0^L \phi^2(x)dx}{\int_0^L D_l(\phi''(x)) - \frac{F}{b}(\phi'(x))^2 dx}\right]^{-1} \tag{16}$$

2.3.1 Effect of Axial Force. Equation (16) relates the normalized dynamic response of the PBP actuator element to the forcing frequency ω and the axial force F_a. In Fig. 6, this response is plotted against the reduced frequency f/f_n. The reduced frequency is the forcing frequency $f=2\pi\omega$, divided by the natural frequency f_n of the plain bimorph actuator element in the pin-pin configuration. When $F_a=0$, the natural frequency peak in the Bode plot occurs, therefore, at $f/f_n=1$. The axial force is normalized with respect to the perfect-column buckling load ($F_1=\pi^2 D_l b/L^2$). At higher axial forces, the natural frequency peak shifts toward the left, which generally translates to a smaller bandwidth of the actuator element. It can be seen that when the axial force approaches the perfect-column buckling load, the natural frequency approaches zero.

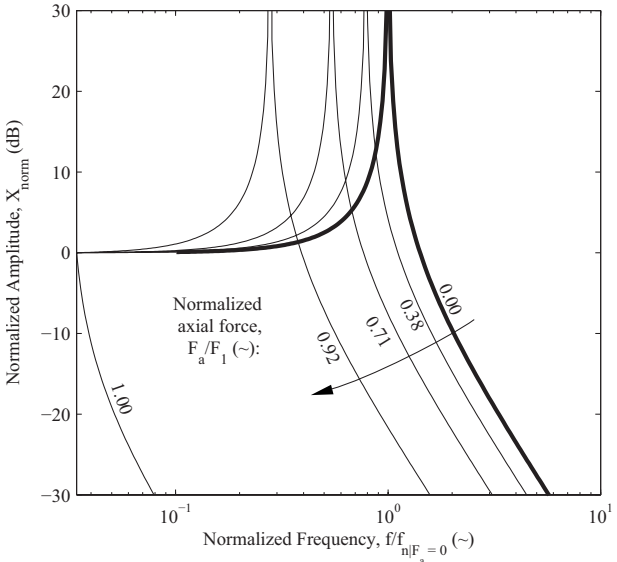

Fig. 6 Effect of axial force on amplitude response of PBP actuator element

What is essentially happening when the axial force is applied is that the stiffness term in Eq. (14) is reduced to zero. In the classic case of vibrating structures, the natural frequency relates linearly to the square root of the stiffness term. When this term is reduced due to the application of an axial force, it is evident that the natural frequency decreases and will eventually reach zero.

2.3.2 Effect of Lumped Inertia. The lumped inertia decreases the first natural frequency of the PBP system of Fig. 5. In Fig. 7, this influence is shown by plotting the normalized natural fre-

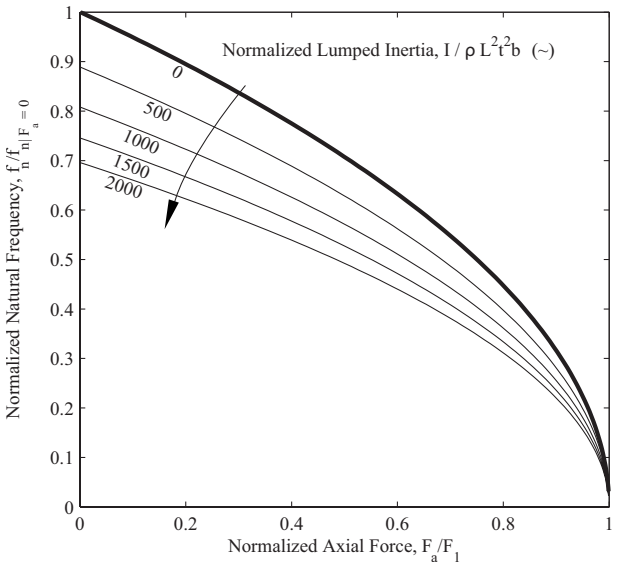

Fig. 7 Effect of lumped inertia on first natural frequency of PBP actuator element

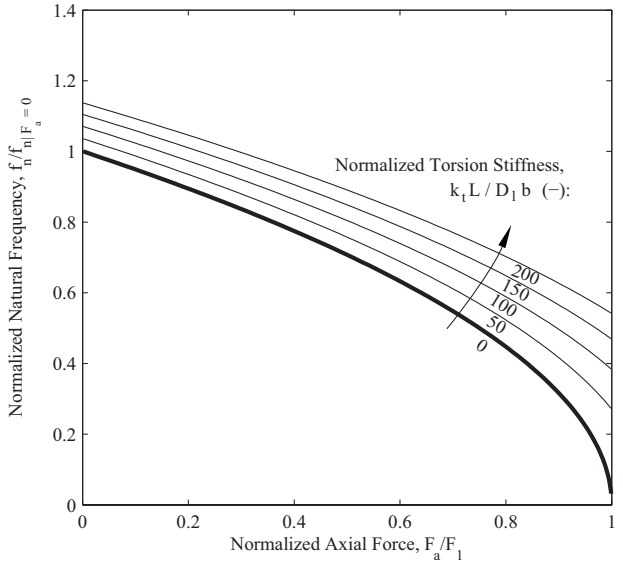

Fig. 8 Effect of torsional stiffness on first natural frequency of PBP actuator element

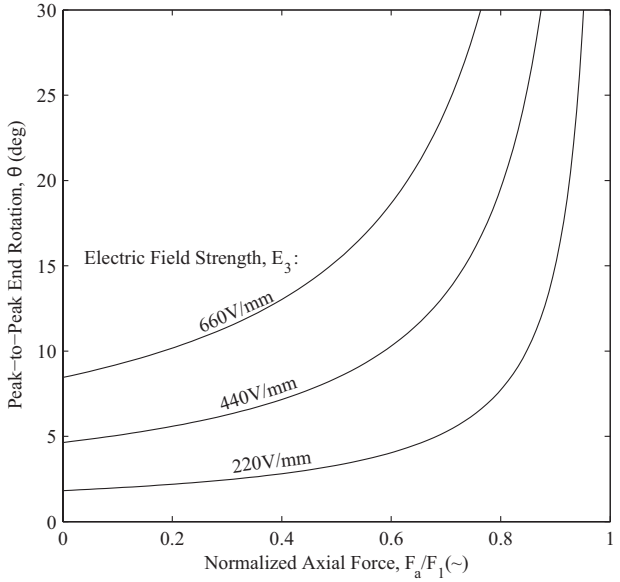

Fig. 9 Relation between end peak-to-peak rotation and axial force for example PBP bimorph actuator element

quency (f/f_n) versus the normalized axial force (F_a/F_1). In accordance with the amplitude response of Fig. 6, the bold line in Fig. 7 shows the decay of the natural frequency with increased axial force. The lumped inertia attached to one of the pivots is normalized with respect to a reference inertia, which is the mass of the actuator multiplied by the cross-sectional area in the xy-plane: $\rho Lbt \times Lt$. It can be seen that the increase in lumped inertia reduces the first natural frequency of the PBP system.

2.3.3 Effect of External Spring. In Fig. 8, the reduced natural frequency versus the normalized axial force is plotted for various values for the torsional spring constant k_t. The bold line represents the default relation for the case that $k_t=0$. This line is the same as the bold line in Fig. 7. The torsional stiffness is normalized with respect to the bending stiffness of the actuator, divided by the element length: $D_l b/L$, which is constant for a PBP element of given dimensions. It can be observed from the lines in Fig. 8 that an increase in the spring constant results in a stiffening of the entire system, and consequently, a higher natural frequency. The addition of a torsional spring can therefore offset the effect of the added inertia and/or the application of the axial force.

2.4 Example PBP Actuator Element. To illustrate the predictions of this model, the reader is asked to consider the simple bimorph piezoelectric actuator element (see Fig. 2), with the dimensions and stiffness properties of Table 1. By employing Eq. (10) with $M_{ex}=0$, the end rotation of this element can be calculated for this element for various values of F_a and E_3. In the present analysis, the following relation for the piezoelectric charge constant and the electric field is employed

$$d_{31} = 1.74 \cdot 10^{-10} + 3.02 \cdot 10^{-16} E_3 \tag{17}$$

It should be noted that the above expression, although accounting for the second-order effects of through thickness field strength, represents the piezoelectric "virgin" curve performance. A complete performance map would include materials-induced hysteresis (and energy dissipation). Such complicated materials-based effects are typically captured from experimental testing because they are dependent upon many factors, including levels of precompression, and accordingly, beyond the scope of this paper. When no external end moment is applied, the positive and negative end rotations are identical in magnitude, and the peak-to-peak end rotation is found by adding those two together (see Eq. (11)). The peak-to-peak end rotation versus the axial force is graphically shown in Fig. 4 for various values of the through-the-thickness electric field. A close match between the lines of Fig. 4 and experimentally obtained data was established by Groen et al. [20]. It can be observed that at 80% of the perfect-column buckling load, the peak-to-peak end rotation is magnified with a factor of 4, with respect to the plain bimorph element.

Table 1 Properties of example PBP element

t_a (μm)	t_s (μm)	t_b (μm)	L (mm)	b (mm)	B_a (kN)	D_l (N m)	$E_{3\max}$ (V/mm)
267	76	102	218	11.2	10.5	3.82	660

The increased end rotation is only beneficial when the blocked moment does not decrease with the same rate. This is exactly where the PBP system differs from the majority of amplification schemes that are used for bimorph actuator elements. In Fig. 9, the so-called design spaces for plain bimorphs are compared with those of PBP actuator elements. The oblique dashed lines represent the relation between the blocked force and end rotation for plain bimorph actuator elements. It is shown how these lines can be shifted through the increase in the electric field. The outer oblique lines form the absolute boundaries between which the bimorph element can operate. From a designer's point of view, it is of interest to determine a bounding box in which every combination of blocked moment and end rotation can be achieved. Such a design space is drawn in Fig. 9 for two values of the electric field. The vertices of this box are positioned on the oblique lines, such that the total surface area of the box is maximized. The growth of the design space is bounded by the maximum electric field that can be applied to the piezoelectric actuator element before depoling.

When an axial force amounting to 85% of the perfect-column buckling load is added to the element, the relation between the blocked moment and end rotation can again be plotted. As can be seen in Fig. 9, much higher end rotations can be sustained for similar blocked end moments. The vertices of the bounding box are, again, positioned, such that the area of the bounding box is maximized. The resulting design space is almost seven times larger than the design space for the plain bimorph piezoelectric element. It can also be observed that the end rotation and blocked moment are increased simultaneously.

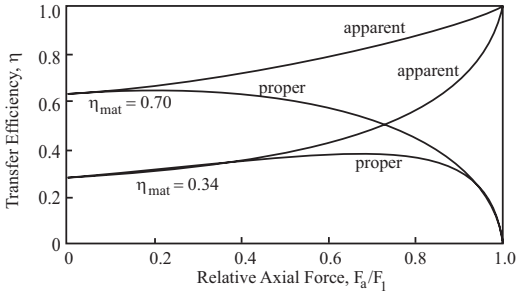

Fig. 10 Transfer efficiency of axially loaded transducer elements [21]

3 Development of PBP Technology

3.1 Early Incarnations of PBP Technology. The first incarnation of PBP technology dates back to 1997 when axial loads were used to counter the inherent stiffness of bimorph PZT transducer elements [13]. This invention was patented in 2001 [21] and it was shown that the apparent transfer efficiency η between the electrical energy input and the mechanical work output approached unity as the axial force on the element increased (see Fig. 10). Contrary to conventional wisdom, it was shown that the transfer efficiency of the precompressed actuator element exceeded the transfer efficiency of the raw piezoelectric material itself.

In 2002, this idea of axially compressing actuators was expanded to the realm of stress-biased unimorph actuators (i.e., RAINBOW®). It was shown that by including an external spring, quasi-static displacements increased with a factor of 4 [22]. Furthermore, it was demonstrated that by applying axial force, the resonance frequency of the actuator elements decreased substantially. Challenges with this approach include the inability of the actuator to take advantage of full positive-to-negative stroke motions along with premature depoling and tensile failure due to adverse loadings of the piezoelectric elements. Also, connectivity to the end effectors is challenging and thickness growth precludes tight packaging. An example of a double unimorph configuration, based on RAINBOW® actuator elements, is presented in Fig. 11.

3.2 Dynamic Elastic Axis Shifting. The increased transfer efficiency resulted in relatively high curvatures in the PBP actuator elements. Since conventional PZT ceramics are sensitive to tensile stresses, these increased curvatures needed to be bounded in order to prevent tensile failure of the convex actuator elements. Traditionally, precompressing of the ceramic elements was done by curing the bimorph laminate at elevated temperatures and relying on the difference in the coefficient of thermal expansion (CTE) between the ceramic and the substrate material [23]. Although this had proven to work well for conventional bimorph piezoelectric actuators, the dramatically increased curvatures of PBP actuator elements often demanded external bump stops to prevent over-rotation and consequent tensile failure of the convex ceramic elements.

In an effort to have an inherent protection mechanism incorporated within the actuator element, the concept of dynamic elastic axis shifting (DEAS) was introduced. This concept relied on the addition of high-stiffness/high-strength facing sheets to either side of the bimorph actuator. These facing sheets were only attached at either end of the actuator and allowed for an air gap to exist between the actuator face and the facing sheet. This air gap was partially filled with a low modulus spacer, attached to the face of the actuator (see Fig. 12). At high curvatures, the facing sheet and the spacer made contact upon which the facing sheets engaged in the carrying part of the tensile loading, thereby, relieving the convex ceramic element [24]. Engagement of the facing sheets essentially shifted the elastic axis of the laminate toward or beyond the face of the convex ceramic element.

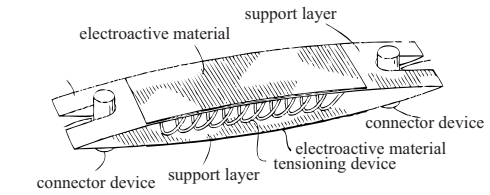

Fig. 11 Axially compressed double unimorph piezoelectric actuator [22]

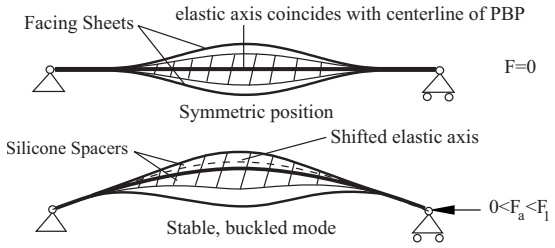

Fig. 12 PBP/DEAS actuator element [24,25]

3.2.1 Predicting First Contact. To aid the designer in predicting the geometry of the actuator at which the engagement of the facing sheet occurs, a simple first-order prediction model is presented. This model was shown to correlate well to experimental results in a previous work by the authors [25]. In Fig. 13, the workings of the facing sheet engagement is presented step by step. In this example, a PBP element is considered with a facing sheet and spacer on the convex face of the actuator element. In a realistic application, one would have the same configuration mirrored in the symmetry plane of the bender element. The following paragraphs describe the step-by-step process and the form factors that are used for the individual components. The reader is cautioned that in this section, the origin of the Cartesian coordinate system has shifted with respect to the coordinate system presented in Sec. 2.

The reader is asked to consider the geometry of the undeflected PBP/facing sheet element of Fig. 13 (top). The dimensions of this arrangement can be captured with three functions: the centerline of the substrate $y_s(x)$, the top face of the spacer $y_{sp}(x)$, and the bottom face of the facing sheet $y_{fs}(x)$. In the undeflected position, the substrate is straight (i.e., $y_s(x)=0$), and the maximum height of the facing sheet is denoted with y_{0fs}. The facing sheet is bonded to the actuator. such that a cosine form factor results. Using the nomenclature of Fig. 13, the vertical coordinate of the facing sheet can be expressed as follows:

$$y_{fs}(x) = \frac{y_{0fs}}{2}\left[1 - \cos\left(\frac{2\pi x}{L_{0sp}}\right)\right] \tag{18}$$

Initial imperfection in the beam is induced by the actuation of the piezoelectric layers of the laminate. When no axial force is applied, this results in a perfect arc form factor for the substrate midplane. When an axial force is applied and one assumes a parabolic form factor for the substrate, which is also a very close approximation to the actual measured shapes of the substrate centerline, then the following relationship is seen between the centerline of the substrate, the horizontal coordinate x, and the end tab rotation angle θ:

$$\tilde{y}_s(x) = \left(x - \frac{x^2}{L_{sp}}\right)\tan\,\theta \tag{19}$$

Note that the tilde above the y coordinates denotes the deflected state of the actuator.

The spacer is assumed to be fully compliant and neither at-

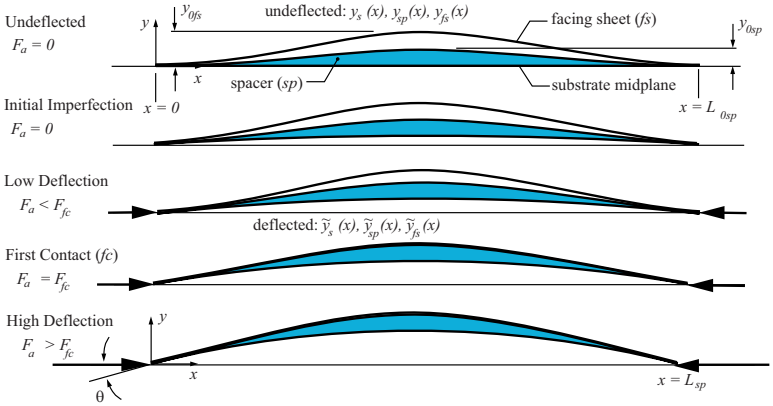

Fig. 13 Schematic representation of facing sheet engagement and definitions [25]

tached to the actuator nor to the facing sheet. During deflection, its thickness is assumed to remain constant. If a cosine form factor is chosen (as is done in the example of the next subsection), this form factor can be added to the deflection of the actuator element (Eq. (19)). The height of the spacer during deflection can consequently be approximated with the following expression:

$$\tilde{y}_{\mathrm{sp}}(x) = y_{\mathrm{sp}}(x) + \tilde{y}_s(x) = \frac{y_{0\mathrm{sp}}}{2}\left[1 - \cos\left(\frac{2\pi x}{L_{\mathrm{sp}}}\right)\right] + \left(x - \frac{x^2}{L_{\mathrm{sp}}}\right)\tan\,\theta \tag{20}$$

From Eq. (20), it can be seen that the height of the upper face of the spacer during deflection is approximated by the height of the spacer with zero deflection y_{sp} and the shape of the substrate centerline during deflection $\tilde{y}_{\mathrm{sp}}$.

If one assumes that at small deflections, the actual mode shapes of the facing sheet, beam, and spacer possess manufacturing irregularities near the edges, making the shapes of the three very similar, then one can assume that contact occurs when the upper surface of the spacer first reaches the y coordinate of the facing sheet at the midpoint of the PBP beam, such that

$$\tilde{y}_{\mathrm{fs}}|_{x=L_{\mathrm{sp}}/2} = \tilde{y}_{\mathrm{sp}}|_{x=L_{\mathrm{sp}}/2} \tag{21}$$

Substituting Eqs. (18) and (20), and keeping in mind that in the buckled mode $L_{0\mathrm{sp}} \rightarrow L_{\mathrm{sp}}$ yields a first-order approximation for contact

$$\tan\,\theta_{\mathrm{fc}} = \frac{4}{L_{\mathrm{sp}}}(y_{0\mathrm{fs}} - y_{0\mathrm{sp}}) \tag{22}$$

From Eq. (22), it can be seen that by this first-order estimation, the end rotation at which first contact occurs θ_{fc} is just a simple function of the air gap between the upper surface of the spacer and the facing sheet, divided by the length of the spacer.

3.2.2 Experimental Investigation and Results. To demonstrate the validity of Eq. (22), a series of test was carried out, which were reported in a paper by Vos and Barret [25]. In this article, an example is presented where a PBP actuator element is equipped with a set of facing sheets that are bonded to small end tabs at either end of the actuator. The relevant dimensions of this actuator and facing sheets are presented in Table 2. In this example, the facing sheet consisted of unidirectional carbon-fiber-reinforced composite that measured only 20% of the actuator width (i.e., 2 mm). Silicone spacers that matched the width of the facing sheets resulted in a total actuator weight increase of only 12% with respect to the baseline actuator. The silicone spacers were manufactured, such that their top face formed a cosine-shape in the xy-plane.

Table 2 Properties of example PBP/DEAS element

t_a (μm)	t_s (μm)	t_b (μm)	b (mm)	L_{sp} (mm)	$y_{0\mathrm{sp}}$ (mm)	$y_{0\mathrm{fs}}$ (mm)	t_{fs} (μm)
191	76	51	10	72	1.8	4.4	69

This actuator element was subjected to four individual field strengths E_3 and subsequently subjected to an increasing axial force. Two sets of experiments were carried out: one with the spacer/facing sheet arrangement in place and one with just the plain PBP actuator element. The results are presented in Fig. 14. It can be seen that at an end rotation of approximately 8.5 deg, the facing sheets engaged, resulting in a higher resistance against the axial load. The prediction of Eq. (22) (8.2 deg) proved to be a good first estimate for the angle of first contact.

The DEAS in PBP actuators made the addition of bump stops obsolete, leading to a simpler, more robust actuator element. In this example, the geometry of the spacer and facing sheets were chosen to have a cosine shape function. However, other facing

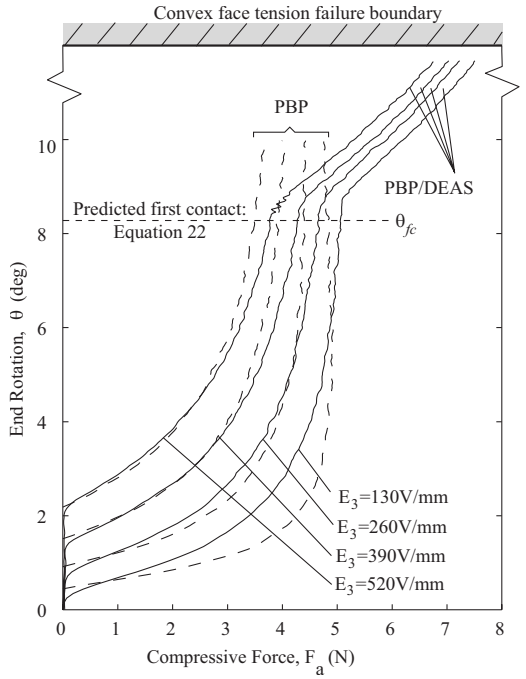

Fig. 14 Stiffening effect due to DEAS in PBP actuator element

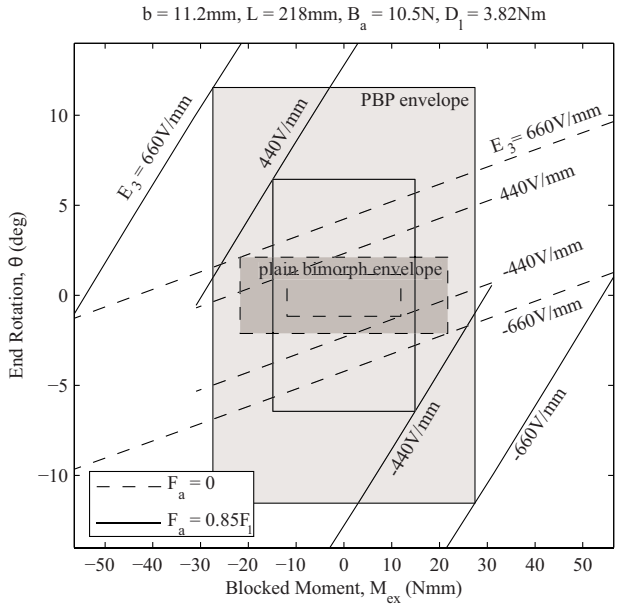

Fig. 15 Increase in design space by switching from plain bimorph piezoelectric actuator to PBP bimorph actuator

sheet/spacer arrangements can be conceived that can induce DEAS in an effective manner. In that case, the model of Sec. 3.2.1 needs to be modified accordingly. The addition of facing sheets has an effect on the quasi-static behavior of PBP elements, in that it introduces additional bounds in the design space of Fig. 15. The addition of facing sheets also has an effect on the dynamic behavior of PBP elements, although that has not (yet) been investigated. One can imagine that the mass addition, as well as the stepwise increase in stiffness, has an effect on the amplitude response of the actuator.

3.3 Snap-Through Behavior

3.3.1 Snap-Through Behavior in Thin Composite Structures. Rather than relying on an axial force for increased mechanical stroke, bistable adaptive composites were developed that showed a significant shape change between the two stable modes [26]. Based on a thin unsymmetrical laminate, piezoelectric patches were positioned, such that they triggered the shape change between two orthogonal bending modes. A substantial amount of research in this area has lead to a good understanding, both experimentally [27] and theoretically [28–30], of the snap-through behavior between the two stable modes. An example of a bistable device, based on piezoelectric macrofiber-composite (MFC) actuators, is presented in Fig. 16. Concepts for morphing wings, based on the bistable adaptive composites, have been proposed, but not yet reduced to practice. Even though significant deformations can be achieved using this concept, its dependance on appropriate boundary conditions can make it difficult to integrate in deforming wing structures.

3.3.2 Snap-Trough Behavior in PBP Class Actuators. The electrical-thermal-mechanical coupling in PBP actuators was investigated extensively in 2007 [31,32]. Close correlations between analytical and numerical models with experimental data were presented. In addition, the realm of bistability in PBP actuator elements was explored both experimentally and theoretically [18]. It was found that by increasing the axial load on the PBP actuator elements, the shape change between positive and negative curvature became essentially instantaneous rather than gradual. This apparent snap-through behavior was uncontrolled, but resulted in relatively high curvatures. It was demonstrated that both applied actuator voltage and boundary conditions are instrumental in determining beyond what the axial load snap-through of the actuator is induced. The experimental setup that yielded these results is presented in Fig. 17.

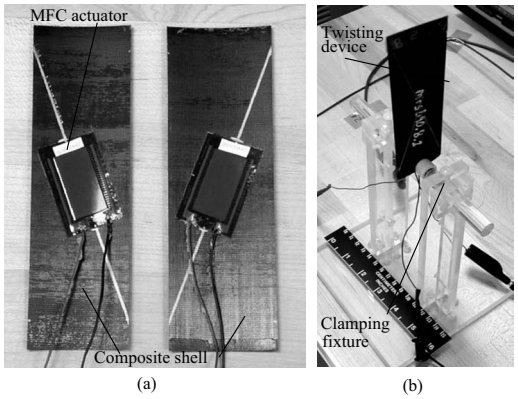

Fig. 16 The active experimental device: placement of the MFC actuators (left) and the assembled device in experimental test fixture (right) [27]

In an effort to increase the mechanical work output in PBP-class actuators, the concept of converse buckling was investigated in 2008 [19]. In post-buckled mode, the distributed moment in the element was inverted, while boundary conditions prevented the element from rotating in the direction of the commanded moment. It was shown that in order to sustain equilibrium, axial loads exceeding the perfect-column buckling load were required. A controlled relaxation of the boundary conditions resulted in an increase in the axial load (close to four times the perfect-column buckling load), followed by a snap-through in the direction of the applied moment. Quasi-static experiments verified that the mechanical work output was increased substantially at elevated axial loads, and close to the perfect-column buckling load bistable behavior was observed [19].

4 PBP Actuators in Aerospace Applications

The application of PBP-class actuators in aerospace applications has successfully demonstrated the viability of this technique outside the laboratorial environment. This section presents a string of examples that were conceived over the past 5 years.

4.1 Application in Subscale VTOL MAV. The first incarnation of PBP actuator technology in flightworthy aircraft was presented in 2005. A vertical-take-off-and-landing (VTOL) subscale microaerial vehicle (MAV) was retrofitted with PBP actuator elements to provide pitch control through grid fins. The integrated actuator element can be seen in Fig. 18 along with an image of the

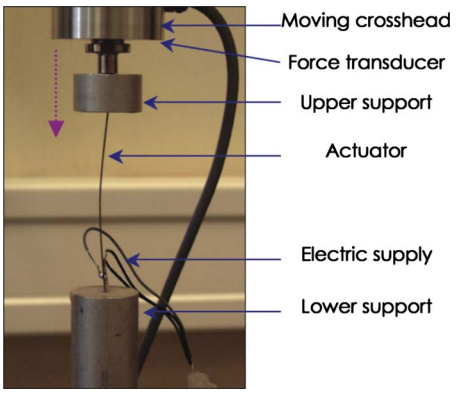

Fig. 17 Experimental setup for PBP snap-through experiment [32]

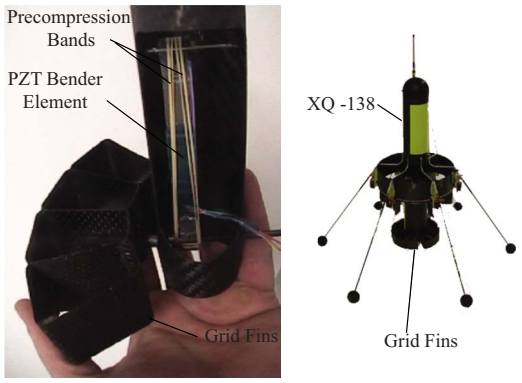

Fig. 18 Application of PBP flight control actuators [14]

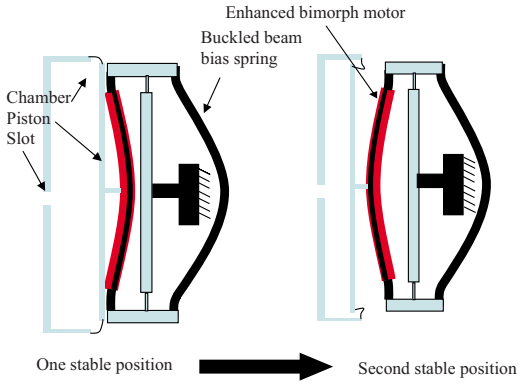

Fig. 20 PBP actuated synthetic jet [39]

subscale MAV. Because the PBP actuators were much simpler and operated as highly efficient solid state actuators, they consumed 0.4% of the power, weighed 87% less, moved seven times faster, and possessed an order of magnitude fewer parts than conventional servoactuators that they replaced. Because they did not employ any linkages or pushrods, their slop levels were reduced by more than 98%. The result of these benefits was that the operating empty weights of the XQ-138 family were enhanced by nearly 4%, while the gross performance was improved in every other measure [16,33,34]. It should be noted, however, that these performance gains were obtained for an example application that was tailored toward the application of PBP actuators. They could therefore differ if applied in other applications. This statement also applies to the subsequent examples in this section.

4.2 Morphing Wing Flight Control. Although morphing wing flight control is relatively straight-forward in subscale UAVs, whenever a membrane wing is used, it can induce challenging requirements on the actuators when a wing section of substantial thickness needs to be deformed [35]. Rather than investing energy in resisting the aerodynamic loads, much energy is lost in straining the passive structure of the wing. To avoid these obstacles, a synergetic approach was taken to incorporate PBP actuator elements in place of ailerons on a 1.4 m span UAV. PBP morphing panels were integrated from the 65% to the 95% of the semispan. The morphing wing panels employed a latex wing skin that was pulled taut between the trailing edge and a tapered D-spar (see Fig. 19). The skin was tailored such as to provide an axial load to the PBP actuator elements that were clamped between the trailing edge and the D-spar.

The PBP elements lead to a weight impact on the total aircraft operating empty weight of only 3 g, as compared with conventional servoactuators, which induced a 59 g weight penalty. Extensive testing demonstrated that deflections could be increased by more than a factor of 2, compared with the baseline bimorph. It was shown that trailing edge angular deflections in excess of 15 deg peak-to-peak could be generated at speeds of up to 34 Hz for under 100 mW of total power consumption. It was shown during the flight that wing morphing could produce 38% more roll control authority and 3.7 times greater control derivatives than conventional approaches [36,37].

Additionally, a semianalytical model, based on the Rayleigh–Ritz method of assumed modes, was developed to predict the amount of wing morphing as a function of the applied electric field on the piezoelectric actuator elements. Aerodynamic loading on the wing was modeled using Theodorson's theory of disturbed flow. The excellent correlation between theory and experiment was demonstrated [17,38].

4.3 Dynamic Tangential Synthetic Jet Actuation. In 2006, a PBP based synthetic jet actuator (Fig. 20) was designed and experimentally tested. By employing an axial force generated by a bent elastic member, it was shown that the mechanical energy output per cycle increased with a factor of 8, compared with the baseline bimorph actuator. The PBP element demonstrated a bidirectional, nearly constant force of 1 N over a displacement of 5.5 mm. The synthetic jet demonstrated peak air velocities of 15 m/s with a duty cycle of 30 Hz. High frequency operation was demonstrated with duty cycles varying between 1 cps and 30 cps [39].

4.4 Miniature Flap Actuation. Miniature MAVs have relatively high flight control system weight fractions because conventional electromechanical flight control actuators do not scale properly. In other words, the flight-control-system weight to operating empty weight ratio increases with decreasing aircraft size. In an effort to decrease the flight system weight, all-moving flight control surfaces were developed back in the 1990s [40]. These control surfaces consisted of a small aeroshell with a fixed pivot rod. A bimorph piezoelectric actuator element acted as a flexible spar and rotated the shell about its pivot. In doing so, it changed the local incidence angle of the control surface, which in turn resulted in a change in lift.

To induce greater deflections of these small control surfaces, a 51 mm span, 25 mm chord subscale aircraft stabilator and PBP actuator element were constructed with a high compression elastomeric band (Fig. 21). It was shown that a simple bender element, which generated only 2.6 deg tip rotations (unloaded), could be retrofitted with an elastic precompression band to increase deflections to nearly fourfold. This PBP-enabled actuator element was integrated into a graphite-epoxy aeroshell and tested quasi-

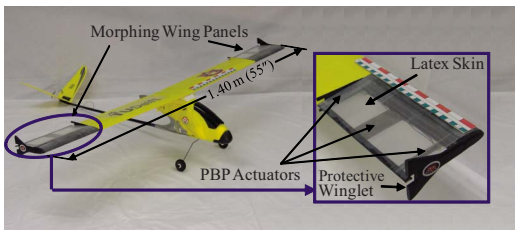

Fig. 19 Subscale UAV employing PBP actuated morphing panels [38]

Fig. 21 PBP actuated flight control surface for micro aerial vehicle [41]

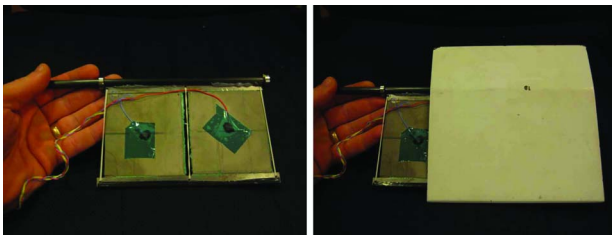

Fig. 22 PBP/DEAS experimental test article actuator core and assembly into aeroshell [42]

statically. Pitch deflections of up to ±25 deg (peak-to-peak) were recorded at field strengths of just 520 V/mm over the 127 μm (5 mil) thick PZT ceramic elements with good correlation between theory and experiment. Wind tunnel testing of the stabilator showed no flutter or divergence tendencies and steady pitch control of up to ±20 deg at speeds, as great as 120 kts [41].

4.5 Transonic Missile Fin. In 2008, a transonic missile fin designed for velocities up to Mach 1.3 was retrofitted with PBP actuator elements within its aeroshell (see Fig. 22). By positioning the elements within the control surface itself, the minimal volume of the missile was occupied by the flight control mechanism. To prevent the elements from excessive curvatures and consequent tensile failure of the convex ceramic elements, DEAS was employed by means of an additional facing sheet layer. Deflection levels in excess of 7 deg were demonstrated at rates through 21 Hz, for less than 1.3 W of peak power. It was shown that theoretical estimations of pitch deflections using the laminated plate theory, kinematics, and imperfection level determination adequately captured the performance of the PBP/DEAS fin [42].

5 Conclusions

An overview of the PBP actuator technology has been presented. A simple model that captures the static behavior of the actuator elements illustrated the increased stroke and work output that resulted from applying an axial force to a simple bimorph piezoelectric actuator element. An analytical model that predicts the amplitude response of PBP elements with forcing frequency has been presented. From its earliest incarnations back in the 1990s till the present day, the PBP actuators have outperformed conventional bimorph piezoelectric actuators in terms of actuator stroke (up to 300% increase) and blocked force capability. Their threefold increase in mechanical work output and relatively simple configuration have made them excellent candidates for flight control applications in subscale UAVs. Examples of successful integration in aerospace systems have been shown in applications ranging from subsonic through supersonic. When properly designed, benefits of using PBP actuator elements over conventional electromechanical servoactuators include a substantial decrease in system weight, an order of magnitude less power consumption and part count, and a substantial increase in bandwidth.

Nomenclature

A = extensional stiffness matrix (N/m)
b = actuator width (m)
B = coupling stiffness matrix (N)
D = bending stiffness matrix (N m)
E = stiffness $\mathrm{N/m^2}$
F = force (N)
L = actuator length (m)
M = applied moment vector or hinge moment (N m)
t = thickness (m)
x = principal direction (m)
X = amplitude response
y = beam displacement in unloaded condition ($F_a=0$) (m)
$\tilde{y}$ = displacement during axial compression ($F_a>0$) (m)
ε = strain
η = transfer efficiency
θ = end rotation (deg)
Θ = normalized end rotation
κ = curvature (deg/m)
Λ = unloaded piezoelectric strain
ϕ = shape function
ψ = displacement offset between $F_a=0$ and $F_a>0$ (m)

Subscripts

0 = undeflected
1 = first buckling mode
1, 2, 3 = laminate coordinates
a = actuator or axial
fc = first contact
fs = facing sheet
l = laminate
n = natural
o = output
$p2p$ = peak to peak
s = substrate
sp = spacer

References

[1] Ehlers, S., and Weisshaar, T., 1990, "Static Aeroelastic Behavior of an Adaptive Laminated Piezoelectric Composite Wing," Proceedings of the 31st AIAA/ASME/ASCE/AHS/ASC Structures, Structural Dynamics and Materials Conference, AIAA Paper No. 90-1078.
[2] Barrett, R., 2004, "Adaptive Aerostructures—The First Decade of Flight on Uninhabited Aerospace Systems," Proceedings of the Society of Photo-Optical Instrumentation Engineers 11th Annual International Symposium on Smart Structures and Materials, Society of Photo-Optical Instrumentation Engineers, Vol. 5388, pp. 190–201.
[3] Xu, W., and King, T., 1996, "Flexure Hinges for Piezoelectric Displacement Amplifiers: Flexibility, Accuracy, and Stress Considerations," J. Soc. Precis. Eng., **19**(1), pp. 4–10.
[4] Samak, D. K., and Chopra, I., 1996, "Design of High Force, High Displacement Actuators for Helicopter Rotors," Smart Mater. Struct., **5**, pp. 58–67.
[5] Prechtl, E. F., and Hall, S. R., 1999, "Design of a High Efficiency, Large Stroke, Electromechanical Actuator," Smart Mater. Struct., **8**, pp. 13–30.
[6] Lee, T., and Chopra, I., 2001, "Design of Piezostack-Driven Trailing-Edge Flap Actuator for Helicopter Rotors," Smart Mater. Struct., **10**(1), pp. 15–24.
[7] Hall, S. R., and Prechtl, E. F., 1996, "Development of a Piezoelectric Servoflap for Helicopter Rotor Control," Smart Mater. Struct., **5**, pp. 26–34.
[8] Jiang, J., and Mockensturm, E., 2006, "A Motion Amplifier Using an Axially Driven Buckling Beam: I. Design and Experiments," Nonlinear Dyn., **43**(4), pp. 391–409.
[9] Jiang, J., and Mockensturm, E., 2006, "A Motion Amplifier Using an Axially Driven Buckling Beam: II. Modeling and Analysis," Nonlinear Dyn., **45**(1–2), pp. 1–14.
[10] Ervin, J. D., and Brei, D., 1998, "Recurve Piezoelectric-Strain-Amplifying Actuator Architecture," IEEE/ASME Trans. Mechatron., **3**, pp. 293–301.
[11] Mtawa, A., Sun, B., and Gryzagoridis, J., 2007, "An Investigation of the Influence of Substrate Geometry and Material Properties on the Performance of the C-Shape Piezoelectric Actuator," Smart Mater. Struct., **16**(4), pp. 1036–1042.
[12] Moskalik, A. J., and Brei, D., 1997, "Quasi-Static Behavior of Individual C-Block Piezoelectric Actuators," J. Intell. Mater. Syst. Struct., **8**(7), pp. 571–587.
[13] Lesieutre, G., and Davis, C., 1997, "Can a Coupling Coefficient of a Piezoelectric Device Be Higher Than Those of Its Active Material?," J. Intell. Mater. Syst. Struct., **8**(10), pp. 859–867.
[14] Vos, R., and Barrett, R., 2010, "Dynamic Elastic Axis Shifting: An Important Enhancement of Postbuckled Precompressed (PBP) Actuators," AIAA J., **48**(3), pp. 583–590.
[15] Jones, R., 1975, "Micromechanical Behavior of a Lamina," *Mechanics of Composite Materials*, 4th ed., Hemisphere, Washington, DC.
[16] Barrett, R., McMurtry, R., Vos, R., Tiso, P., and DeBreuker, R., 2005, "Post-Buckled Precompressed (PBP) Elements: A New Class of Flight Control Actuators Enhancing High Speed Autonomous VTOL MAVS," Proceedings of the Society of Photo-Optical Instrumentation Engineers 12th Annual International Symposium on Smart Structures and Materials, Society of Photo-Optical

Instrumentation Engineers, Vol. 5762, pp. 111–122.
[17] DeBreuker, R., Tiso, P., Vos, R., and Barrett, R., 2006, "Nonlinear Semi-Analytical Modeling of Postbuckled Precom-Pressed (PBP) Piezoelectric Actuators for UAV Flight Control," Proceedings of the 47th AIAA/ASME/ASCE/AHS/ASC Structures, Structural Dynamics and Materials Conference, AIAA Paper No. 2006-1795.
[18] Giannopoulos, G., 2007, "Large Displacement Piezoelectric Structures for Actuation Applications," Ph.D. thesis, Vrije Universiteit Brussel, Brussel, Belgium.
[19] Vos, R., Barrett, R., and Zehr, D., 2008, "Magnification of Work Output of PBP Class Actuators Using Buckling/Converse Buckling Techniques," Proceedings of the 49th AIAA/ASME/ASCE/AHS/ASC Structures, Structural Dynamics and Material Conference, Paper No. AIAA-2008-1705.
[20] Groen, M., VanSchravendijk, M., Barrett, R., and Vos, R., 2009, "Advanced Control Techniques for Post-Buckled Precompressed (PBP) Flight Control Actuators," Proc. SPIE, **7288**, p. 72881V.
[21] Lesieutre, G., and Davis, C., 2001, "Transducer Having a Coupling Coefficient Higher Than Its Active Material," U.S. Patent No. 6,236,143.
[22] Schwartz, R. W., and Narayanan, M., 2002, "Electroactive Apparatus and Methods," Clemson University, International Patent No. PCT/US02/09698.
[23] Barrett, R., 1992, "Active Plate and Wing Research Using EDAP Elements," Smart Mater. Struct., **1**(3), pp. 214–226.
[24] Barrett, R., and Tiso, P., 2005, "PBP Adaptive Actuator Device and Embodiments," Delft University of Technology, International Patent No. PCT/NL2005/000054.
[25] Vos, R., and Barrett, R., 2007, "Dynamic Elastic Axis Shifting: An Important Enhancement of Postbuckled Precom-Pressed (PBP) Actuators," Proceedings of the 48th AIAA/ASME/ASCE/AHS/ASC Structures, Structural Dynamics and Material Conference, Paper No. AIAA-2007-1705.
[26] Dano, M. L., and Hyer, M. W., 2003, "SMA-Induced Snap-Thru of Unsymmetric Fiber-Reinforced Composite Laminates," Int. J. Solids Struct., **40**(22), pp. 5949–5972.
[27] Schultz, M. R., and Hyer, M. W., 2003, "Snap-Through of Unsymmetric Cross-Ply Laminates Using Piezoceramic Actuators," J. Intell. Mater. Syst. Struct., **14**(12), pp. 795–814.
[28] Ren, L., 2007, "Theoretical Study on Shape Control of Thin Cross-Ply Laminates Using Piezoelectric Actuators," Compos. Struct., **80**(3), pp. 451–460.
[29] Gude, M., and Hufenbach, W., 2006, "Design of Novel Morphing Structures Based on Bistale Composites With Piezoceramic Actuators," Mech. Compos. Mater. Struct., **42**(4), pp. 339–346.
[30] Schultz, M. R., Hyer, M. W., Williams, R. B., Wilkie, W. K., and Inman, D. J., 2006, "Snap-Through of Unsymmetric Laminates Using Piezocomposite Actuators," Compos. Sci. Technol., **66**(14), pp. 2442–2448.
[31] Giannopoulos, G., Monreal, J., and Vantomme, J., 2007, "Snap-Through Buckling Behavior of Piezoelectric Bimorph Beams: I. Analytical and Numerical Modeling," Smart Mater. Struct., **16**(4), pp. 1148–1157.
[32] Giannopoulos, G., Monreal, J., and Vantomme, J., 2007, "Snap-Through Buckling Behavior of Piezoelectric Bimorph Beams: II. Experimental Verification," Smart Mater. Struct., **16**(4), pp. 1158–1163.
[33] Barrett, R., Vos, R., Tiso, P., and DeBreuker, R., 2005, "Post-Buckled Precompressed (PBP) Actuators: Enhancing VTOL Autonomous High Speed MAVS," Proceedings of the 46th AIAA/ASME/ASCE/AHS/ASC Structures, Structural Dynamics and Materials Conference, AIAA Paper No. 2005-2113.
[34] Barrett, R., McMurtry, R., Vos, R., DeBreuker, R., and Tiso, P., 2006, "Post-Buckled Precompressed Piezoelectric Flight Control Actuator Design Development and Demonstration," Smart Mater. Struct., **15**(5), pp. 1323–1331.
[35] Bilgen, O., Kochersberger, K., Diggs, E., Kurdila, A., and Inman, D., 2007, "Morphing Wing Micro-Air-Vehicles via Macro-Fiber-Composite Actuators," Proceedings of the 48th AIAA/ASME/ASCE/AHS/ASC Structures, Structural Dynamics, and Materials Conference, Paper No. AIAA-2007-1785.
[36] Vos, R., Barrett, R., Krakers, L., and van Tooren, M., 2006, "Post-Buckled Precompressed (PBP) Piezoelectric Actuators for UAV Flight Control," Proceedings of the Society of Photo-Optical Instrumentation Engineers 13th Annual International Symposium on Smart Structures and Materials, Society of Photo-Optical Instrumentation Engineers, Vol. 6173.
[37] Vos, R., Barrett, R., DeBreuker, R., and Tiso, P., 2007, "Post-Buckled Precompressed (PBP) Elements: A New Class of Control Actuators for Morphing Wing UAVs," Smart Mater. Struct., **16**(3), pp. 919–926.
[38] Vos, R., DeBreuker, R., Barrett, R., and Tiso, P., 2007, "Morphing Wing Flight Control via Post-Buckled Precompressed Piezoelectric Actuators," J. Aircr., **44**(4), pp. 1060–1068.
[39] Clingman, D. J., 2006, "Development of an Aerodynamic Synthetic Jet Actuator Based on a Piezoceramic Buckled Beam," MS thesis, University of Maryland, College Park, MD.
[40] Barrett, R., 1996, "Active Aeroelastic Tailoring of an Adaptive Flexspar Stabilator," Smart Mater. Struct., **5**(6), pp. 723–730.
[41] Barrett, R., Vos, R., and DeBreuker, R., 2007, "Post-Buckled Precompressed (PBP) Subsonic Micro Flight Control Actuators and Surfaces," Proceedings of the Society of Photo-Optical Instrumentation Engineers 14th Annual International Symposium on Smart Structures and Materials, Society of Photo-Optical Instrumentation Engineers, Vol. 6525.
[42] Barrett, R., and Vos, R., 2008, "Design, Development and Testing of a Transonic Missile Fin Employing PBP/DEAS Actuators," Proceedings of the Society of Photo-Optical Instrumentation Engineers 11th Annual International Symposium on Smart Structures and Materials, Society of Photo-Optical Instrumentation Engineers, Vols. 6930–6937.